Stability of Slopes Loaded Over a Finite Area

LESLIE L. KARAFIATH and EDWARD A. NOWATZKI,
Grumman Aerospace Corporation, Bethpage, New York

In frictional soils, when pore pressures are negligible, failure occurs in shear zones. In such cases the stability of slopes loaded over a finite area can be analyzed by bearing capacity methods. Two methods of analysis are presented: an approximate method, based on the assumption that a slip-line field analogous to the Prandtl solution for horizontal ground applies, and a numerical method, based on the numerical integration of the governing differential equations of plastic equilibrium. A formula for the N_q value is given for the slope angle, friction angle, and the angle of the inclination of load and surcharge as principal variables. The concept of stress gradient, which expresses the rate of increase of the bearing stress from the edge of the loaded area, is used to account for the effect of the weight of the soil. The stress gradients obtained by the approximate method are compared with those determined from bearing stresses obtained by numerical integration methods. Results of small-scale experiments are presented showing that the decrease of bearing capacity with slope angle can be reasonably estimated by the approximate method. The methods apply to the stability analyses of highway embankments as well as to problems in land locomotion theory.

•TYPICAL EXAMPLES of slopes loaded over a finite area are shown in Figure 1. These problems of slope stability differ from that of the stability of foundations embedded in a slope investigated by Meyerhof (1) in that the loading is at the surface.

METHODS OF ANALYSIS

The stability of slopes is usually analyzed by assuming various potential sliding surfaces and determining the most critical one by trial and error. For clays and silts the transfer of pore water from the less stressed zones to the most stressed locations results in the development of a single failure surface. Consequently, the trial and error approach to the analysis of the stability of silt and clay slopes is reasonable.

In unsaturated frictional soils, failure is generally not restricted to a single failure surface but occurs in zones of plastic failure. It is for such conditions that the method of analysis presented in this paper applies. The equilibrium of granular masses, in which no significant pore pressures develop upon loading, is governed by the differential equations of plastic equilibrium. The solution of these differential equations is a slip-line field, a classic example of which is the Prandtl slip-line field for loading on a horizontal surface of a weightless soil.

All analyses presented herein assume that failure upon loading occurs in shear zones, with plastic equilibrium conditions prevailing at every point within these zones. Two methods are applied in the analysis: an approximate method that assumes stress fields analogous to the Prandtl solution in the slopes, and a numerical method based on the

Paper sponsored by Committee on Embankments and Earth Slopes and presented at the 49th Annual Meeting.

numerical integration of the governing partial differential equations. Notation used in the analyses is defined in the Appendix.

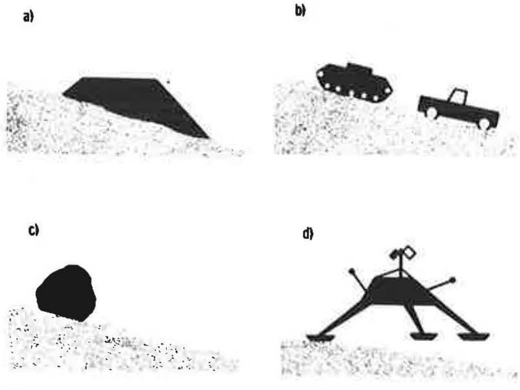

Figure 1. Examples of slopes loaded over a finite area at their surface: (a) highway embankment, (b) off-the-road vehicles, (c) lunar boulder, and (d) landing space vehicle.

ANALYSIS THAT ASSUMES FAILURE ZONES ANALOGOUS TO PRANDTL'S SOLUTION

The failure zones assumed in this analysis consist of a wedge in the active Rankine state (I, Fig. 2), a radial shear zone (II, Fig. 2) bounded by a logarithmic spiral, and a wedge in the passive Rankine state (III, Fig. 2). Both the active and passive wedges correspond to the state of stresses in an infinite slope. The pole of the logarithmic spiral that bounds the radial shear zone is assumed at the outer edge of the loaded area (point A, Fig. 2), thereby ensuring continuity of the slip lines and their tangents throughout the shear zones.

The angles of the active and passive wedges, θ_1 and θ_2 in Figure 2, can be determined (2) from the following:

$$\theta_1 = \tfrac{1}{2}\left[\frac{\pi}{2} + \varphi - (\delta + \epsilon) - \arcsin\frac{\sin(\delta + \epsilon)}{\sin\varphi}\right] \quad \text{when} \quad (\delta + \epsilon) \le \varphi \tag{1}$$

$$\theta_2 = \tfrac{1}{2}\left[\frac{\pi}{2} - \varphi - (\lambda + \epsilon) + \arcsin\frac{\sin(\lambda + \epsilon)}{\sin\varphi}\right] \quad \text{when} \quad (\lambda + \epsilon) \le \varphi \tag{2}$$

(For vertical surcharge only, as in Figure 2, $\lambda = 0$.) The central angles of the radial shear zone are

$$\beta_1 = \theta_1 + \epsilon - \varphi$$

and (3)

$$\beta_2 = \frac{\pi}{2} - \theta_2 - \epsilon$$

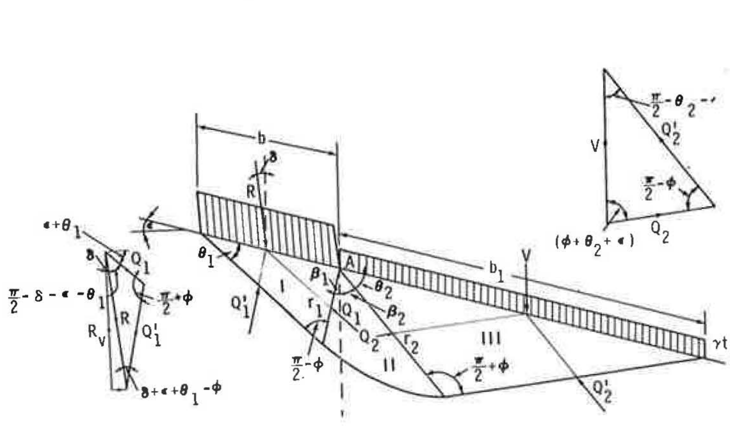

Figure 2. Shear zone geometry for sloping surface analogous to Prandtl's solution.

If the weight of the soil is disregarded and cohesion is zero, the bearing capacity can be expressed as

$$q_{uv} = pN_q \tag{4}$$

The N_q factor is determined from the equilibrium of moments about point A. For a uniform surcharge, the distribution of stresses at the sides of the active and passive wedges is uniform, and the resultants of these stresses, Q_1 and Q_2, act at the middle of these sides. All forces can be determined from the vector diagrams of Figure 2. Because the resultant of the stresses acting on the logarithmic spiral passes through the pole, $Q_1 \cos\varphi(r_1/2) = Q_2 \cos\varphi(r_2/2)$. After substitutions and rearrangements,

$$N_q = \frac{\cos(\lambda + \epsilon + \theta_2)\cos\delta\sin\theta_1}{\sin(\delta + \epsilon + \theta_1 - \varphi)\cos(\varphi + \theta_2)\cos\lambda}\, e^{2(\beta_1 + \beta_2)\tan\varphi} \tag{5}$$

Figure 3 shows the N_q values for vertical loading and slopes varying from $\epsilon = 0$ to $\epsilon = 30$ deg.

For the determination of the effect of cohesion, the relationship $N_c = (N_q - 1)\cot\varphi$ used by Terzaghi and others in bearing capacity formulas for level ground is only approximately valid. For the case of sloping ground, cohesion can be taken into account by using reduced stresses, which are the vectorial sum of ψ and the surcharge or bearing stresses. The reduced stresses are indicated by primes in Figure 4. Equation 4 is valid for the primed stresses and the N_q value can be calculated for any inclination of the reduced bearing stress from Eq. 5. The inclination of the reduced surcharge and bearing stresses can be determined from the vector diagrams in Figure 4.

Equation 5, derived on the basis of a slip-line field for weightless soil, is also valid if the soil possesses weight. This follows from the numerical solution of the governing differential equations presented in the next section where the stresses at the singular point A are computed as if that point were a degenerated logarithmic spiral, the same as in the Prandtl solution. The part of the bearing stress that is uniformly distributed is due to the surcharge, whereas the part that increases with the distance from the edge of the loading is due to the weight of the soil. The stress at point A is equal to the uniformly distributed part; therefore, it is the same in both solutions.

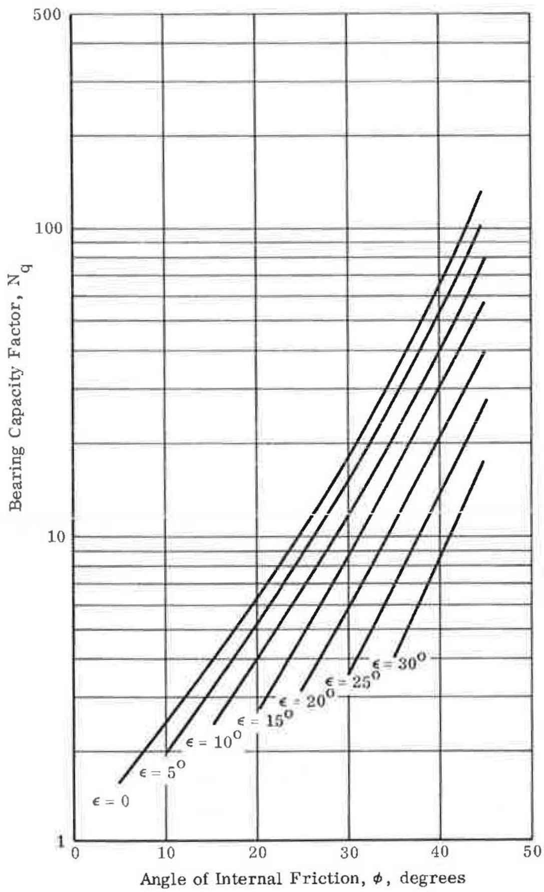

Figure 3. Bearing capacity factor, Nq, for sloping ground and vertical strip-loading ($\lambda = \delta = 0$).

To consider the effect of the weight of the soil, it is assumed that it acts on the slip-line field used for the determination of the N_q value without changing the directions of the slip lines. This assumption is necessary in order to arrive at a closed form solution; the change of

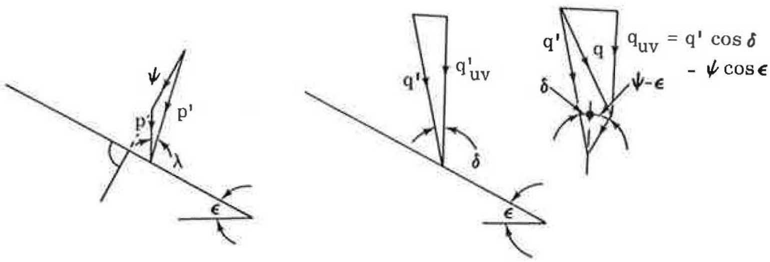

Figure 4. Force diagrams for the determination of reduced stresses.

the slip-line field resulting from the weight of soil is investigated in the next section by numerical integration methods. In a previous study (3), N_γ factors were determined on the basis that the point of attack of the resultant bearing force is such that it meets the equilibrium requirements of the active wedge on which the weight forces act (Fig. 5a). Further studies showed that it is possible to meet the equilibrium requirements for other locations of the resultant bearing force if splitting of the active wedge along the slip lines into two wedges is permitted (Fig. 5b) and the forces resulting from the weight of soil are balanced by triangular bearing stresses. This leads to the concept of stress gradient, i. e., the rate of increase of normal bearing stresses resulting from the effect of weight of the soil (Fig. 6).

In the case of a loaded slope, the stress gradient at the downslope part of the loaded area is different from that at the upslope part. The two stress gradients determine the triangular loading that the soil can ultimately carry due to its own weight. These stress gradients are determined as follows.

The active wedge of the slip-line field used for the determination of the N_q value (Fig. 2) is divided into two smaller wedges along the slip lines (Fig. 5b). The common point of the two wedges (point C in Fig. 5b) is determined by the condition that the bearing stress at this point computed from either wedge be equal. The location of this point is not known beforehand; it is determined from the stress gradients, which are independent of the width of the wedges.

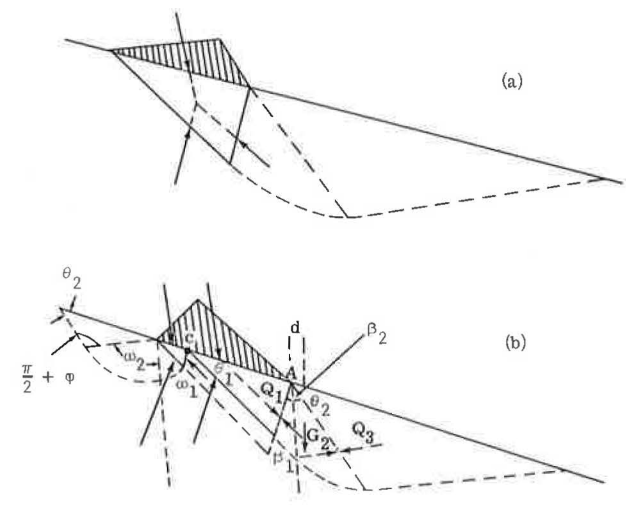

Figure 5. Effect of weight of soil: (a) stress distribution compatible with weight forces acting on the whole active wedge; (b) stress distribution assuming two active wedges corresponding to downslope and upslope failure.

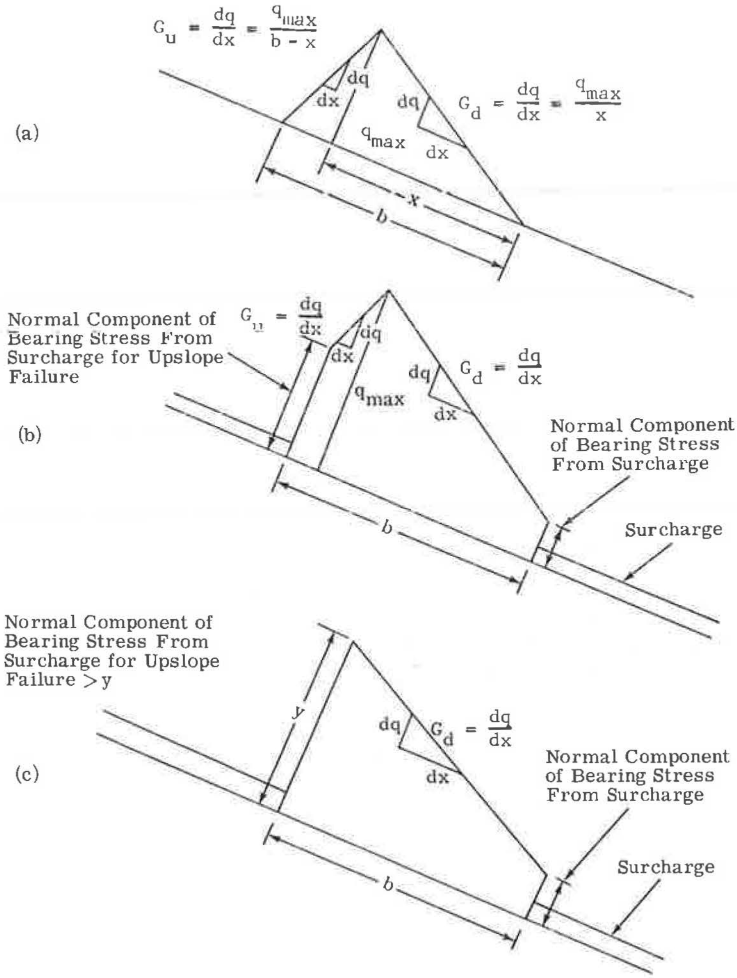

Figure 6. Distribution of bearing stresses: (a) no surcharge; (b) surcharge–upslope and downslope failure; and (c) surcharge–downslope failure only.

For the computation of the upslope gradient, however, the θ_1 and θ_2 angles are replaced by angles ψ_1 and ψ_2, and the β_1 and β_2 angles are replaced by angles ω_1 and ω_2. The values of these angles are

$$\psi_1 = \theta_1 \qquad \psi_2 = \frac{\pi}{2} - \varphi - \theta_2 \tag{6}$$

$$\omega_1 = \frac{\pi}{2} - \psi_1 - \epsilon \qquad \omega_2 = \frac{\pi}{2} + \epsilon - \psi_2 \tag{7}$$

The resultant bearing force R is determined on the basis of equilibrium considerations similar to those used in the determination of N_q. The stresses at the sides of the passive wedge and the radial shear zone increase linearly, and the point of attack of the resultant of these stresses is at the lower third of the sides. The resultant of the stresses acting on the logarithmic spiral portion passes through point A; therefore, it need not be considered. Other acting forces are Q_1, Q_3, and the weight of the radial shear zone G_2. The moment equilibrium about point A for the forces acting on the radial shear zone is expressed as

$$-(Q_1) \cos \varphi \, \frac{2}{3} r_1 + dG_2 + Q_3 \cos \varphi \frac{2}{3} r_2 = 0 \tag{8}$$

From the vector diagram in Figure 2, the resultant bearing force is

$$R = Q_1 \frac{\sin (\pi/2 + \varphi)}{\sin (\delta + \theta_1 + \epsilon - \varphi)} \tag{9}$$

After substitutions and rearrangements, the downslope stress gradient can be expressed as

$$G_d = \gamma \frac{\dfrac{\sin^2 \theta_1}{\cos^2 \varphi} \cdot A + \dfrac{\sin^2 \theta_1 \sin \theta_2 \cos (\theta_2 + \epsilon) \, e^{3(\beta_1 + \beta_2) \tan \varphi}}{\cos \varphi \cos (\varphi + \theta_2)}}{\sin (\delta + \theta_1 + \epsilon - \varphi) \sec (\delta + \epsilon)} \tag{10}$$

where

$$A = \frac{1}{9 \tan^2 \varphi + 1} (3 \tan \varphi \sin \beta_2 - \cos \beta_2) \cdot e^{3(\beta_1 + \beta_2) \tan \varphi}$$
$$+ (3 \tan \varphi \sin \beta_1 + \cos \beta_1) \tag{11}$$

The upslope stress gradient, computed similarly, is

$$G_u = \gamma \frac{\dfrac{\cos^2 (\varphi - \psi_1)}{\cos^2 \varphi} \cdot A' + \dfrac{\cos^2 (\varphi - \psi_1) \sin \varphi_2 \cos (\epsilon - \psi_2)}{\cos \varphi \sin \theta_2} e^{3(\omega_1 + \omega_2) \tan \varphi}}{\cos (\delta + \epsilon + \psi_1) \sec (\delta + \epsilon)} \tag{12}$$

where A' is computed by replacing β_1 and β_2 by ω_1 and ω_2 in Eq. 11. Figure 7 shows G_d/γ and G_u/γ for vertical loadings and slopes ranging from $\epsilon = 0$ to $\epsilon = 30$ deg.

The equations for the stress gradients can also be conveniently used to determine the effect of the weight of soil on the bearing capacity in the case of level ground and inclined loading. In this case $\epsilon = 0$, and downslope and upslope mean in and opposite to the direction of loading respectively. If there is no surcharge, the maximum bearing stress is at a distance (Fig. 6a)

$$x = \frac{G_u}{G_d + G_u} b \tag{13}$$

from the downslope edge of the loading. Its normal component is

$$q_{max} = \frac{G_u G_d}{G_u + G_d} b \tag{14}$$

The average of the normal component of the bearing stress in the two-dimensional case is $q_{av} = \frac{1}{2} q_{max}$; for the axially symmetric case, it is $q_{av} = \frac{1}{3} q_{max}$. Note that the ratio of the average bearing stress in the axially symmetric case to that in the two-dimensional case is 0.66, which approximately corresponds to the 0.6 shape factor for average bearing stresses suggested by Terzaghi. Thus, if the method of stress gradients is used, it is not necessary to consider shape factors for the various types of three-dimensional loadings. This is particularly advantageous when the loading of slopes is considered, because shape factors for this case have not yet been experimentally established.

In the case of a surcharge, the stress gradients expressing the effect of the weight of the soil on the load-bearing capacity have to be used in conjunction with the uniformly

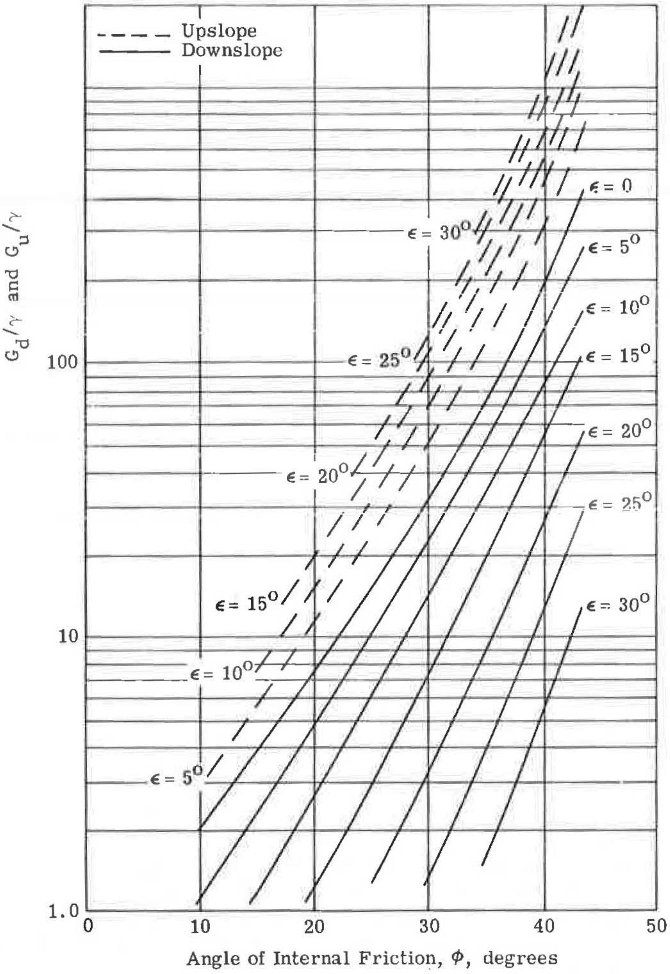

Figure 7. Stress gradients for vertical loading and for slopes varying from $\epsilon = 0$ to $\epsilon = 30$ deg.

distributed bearing stress resulting from the surcharge. Figure 6 shows the distribution of bearing stresses for such cases.

ANALYSIS BY NUMERICAL INTEGRATION METHODS

For the analysis of plastic equilibrium in slopes, the x-axis of the coordinate system is chosen to coincide with the surface of the slope, and the positive z-axis is set perpendicular and downward from it. The differential equations of the slip lines in this coordinate system (4) are

$$
\begin{aligned}
dz &= dx \tan(\theta \pm \mu) \\
d\sigma \pm 2\sigma \tan\varphi d\theta &= \frac{\gamma}{\cos\varphi}\left[\sin(\epsilon \pm \varphi)\, dx + \cos(\epsilon \pm \varphi)\, dr\right]
\end{aligned}
\qquad (15)
$$

The upper sign refers to the family of the slip lines corresponding to the first, and the lower sign corresponds to the second characteristics of the differential equations.

For numerical computations, these differential equations are replaced by the following finite difference equations:

$$x_{i,j} = \frac{z_{i-1,j} - z_{i,j-1} + \alpha_1 x_{i,j-1} - \alpha_2 x_{i-1,j}}{\alpha_1 - \alpha_2}$$

$$z_{i,j} = z_{i-1,j} + \alpha_2\left(x_{i,j} - x_{i-1,j}\right)$$

$$\sigma_{i,j} = \frac{\gamma\left(C\sigma_{i,j-1} + D\sigma_{i-1,j}\right) + 2\sigma_{i,j-1}\sigma_{i-1,j}\left[1 + \left(\theta_{i,j-1} - \theta_{i-1,j}\right)\tan\varphi\right]}{\sigma_{i,j-1} + \sigma_{i-1,j}} \quad (16)$$

$$\theta_{i,j} = \frac{\sigma_{i,j-1} - \sigma_{i-1,j} + 2\tan\varphi\left(\sigma_{i,j-1}\theta_{i,j-1} + \sigma_{i-1,j}\theta_{i-1,j}\right) + \gamma(D - C)}{2\tan\varphi\left(\sigma_{i,j-1} + \sigma_{i-1,j}\right)}$$

where

$x_{i,j}$, $z_{i,j}$ = coordinates of the subscripted modal point (Fig. 8),

$\alpha_1 = \tan\left(\theta_{i,j-1} + \mu\right)$,

$\alpha_2 = \tan\left(\theta_{i-1,j} - \mu\right)$,

$C = \dfrac{\sin(\epsilon - \varphi)}{\cos\varphi}\left(x_{i,j} - x_{i-1,j}\right) + \dfrac{\cos(\epsilon - \varphi)}{\cos\varphi}\left(z_{i,j} - z_{i-1,j}\right)$, and

$D = \dfrac{\sin(\epsilon + \varphi)}{\cos\varphi}\left(x_{i,j} - x_{i-1,j}\right) + \dfrac{\cos(\epsilon + \varphi)}{\cos\varphi}\left(z_{i,j} - z_{i-1,j}\right)$.

These difference equations permit the computation of the coordinates of a nodal point (intersection of slip lines), as well as the values of σ and θ at that point, from the known values at neighboring nodal points having lesser subscripts.

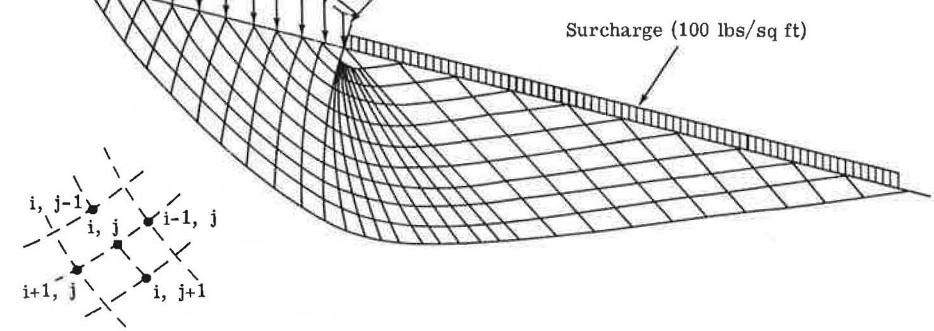

Figure 8. Slip-line field for φ = 35 deg, γ = 100 lb/cu ft, ϵ = 15 deg, p = 100 lb/sq ft determined by numerical integration.

The slip-line field in the passive zone can be computed by equations starting with the boundary values given at the surface of the slope. In the radial shear zone, the same equations are used, but special consideration is given to the central point where the second family of slip lines converge. This point is a degenerated slip line, where θ changes from the value at the passive zone boundary to that specified at the active zone boundary. The total change in θ is divided by the number of slip lines converging at this point to result in an equal $\Delta\theta$ increment between two adjacent slip lines. The σ values for each increment are computed from the equation $\sigma = \sigma_o e^{2(\theta-\theta_o)\tan\varphi}$, which is the solution of the differential equations of Eqs. 15 if both dx and dz vanish. With these θ and σ values assigned to each slip line at this point, the coordinates as well as the σ and θ values for all other points in the radial shear zone can be computed by Eqs. 16. In the active zone the same equations are used except for the points at the loaded surface where $z = 0$ and θ is given. Here x and σ are computed from

$$x_{i,j} = \left(z_{i,j} - z_{i-1,j}\right) \cot\left(\theta_{i-1,j} - \mu\right) + x_{i-1,j}$$

$$\sigma_{i,j} = 2\sigma_{i-1,j}\left(\theta_{i,j} - \theta_{i-1,j}\right) \tan\varphi + \gamma C + \sigma_{i-1,j}$$

The numerical computations were programmed for a GE Mark II computer. An example of the computed slip-line field is shown in Figure 8 for γ = 100 lb/cu ft, φ = 35 deg, ϵ = 15 deg, and p_o = 100 lb/sq ft. The stress at the upslope edge of the loading is less than the bearing stress at this point for upslope failure resulting from the surcharge; therefore, no upslope slip-line field develops.

Note that the slip-line fields representing the solution of the differential Eqs. 15 are geometrically similar only if the ratio

$$R = \frac{P}{\gamma \ell} \tag{17}$$

is the same (where ℓ = any length characteristic of the field, e.g., width of loaded area). Therefore, if the width of the loaded area is given, the slip-line field will change with the magnitude of the surcharge. For weightless soil, $R = \infty$ and the slip-line field assumed in the preceding section is valid; for no surcharge, $R = 0$. The stress gradients determined from the bearing stresses obtained with the numerical solution will also vary with the surcharge. Therefore, the stress gradients computed by the approximate method are not immediately comparable with those computed by the numerical method.

For the case of no surcharge, the numerical method described does not apply because of the nature of the singularity at point A. To obtain a stress gradient closely approximating the surface loading, computer runs were made for a small p of 100 lb/sq ft surcharge. A comparison of stress gradients obtained by the approximate and numerical methods is given in Table 1. Further investigations are planned to determine whether improvements in the numerical procedure (such as using an average value of θ between point i, j and either i-1, j or i, j-1) or other iteration procedures would appreciably affect the value of the computed stress gradients.

TABLE 1

COMPARISON OF STRESS GRADIENTS DETERMINED BY THE APPROXIMATE AND NUMERICAL METHOD

φ (deg)	$\epsilon = 0$		Downslope Gradient (ϵ = 15 deg)	
	Approximate Method ($R = \infty$)	Numerical Method ($R = 0.1$)	Approximate Method ($R = \infty$)	Numerical Method ($R = 0.2$)
20	7.6	3.4	1.1	0.5
25	15.1	6.8	3.1	1.5
30	31.2	14.8	7.3	3.9
35	68.7	36.0	16.8	9.1
40	164.5	71.0	40.6	20.5
45	443.6	166.0	106.0	50.1

RESULTS OF EXPERIMENTS

A series of load tests was performed with circular plates on sand from Jones Beach. The grain size distribution of this sand is shown in Figure 9, and Figure 10 shows the results of triaxial tests run in

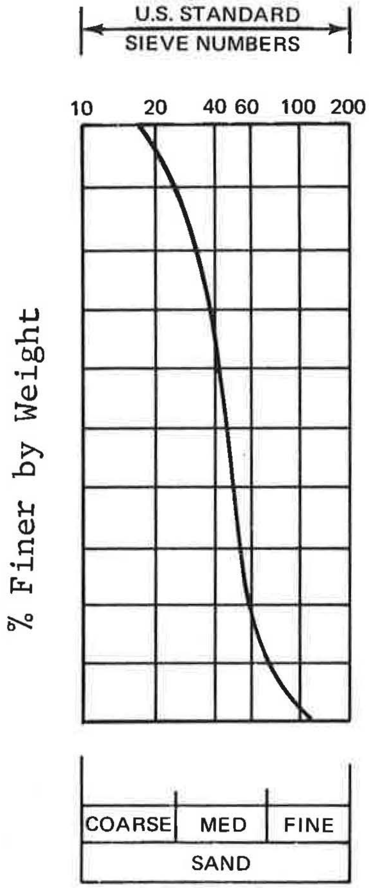

Figure 9. Grain size distribution of Jones Beach sand.

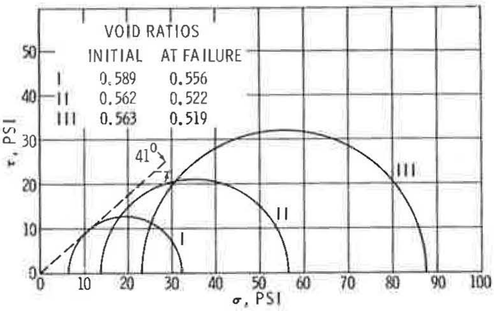

Figure 10. Results of triaxial tests on Jones Beach sand.

an air-dry condition. The volume changes were determined from vertical and circumferential deformation. The sand bed was prepared by using a movable hopper with a rotating distributor cylinder that deposited the sand at densities from 102.5 to 104 lb/cu ft; higher densities were obtained by vibrating the individual layers.

Preliminary tests showed that slanting an originally horizontal box did not result in the stress conditions desired, even if the side walls were lubricated. It was found satisfactory, however, to deposit the material in sloping layers, and this method was adopted for the tests. The vertical load was transmitted to the circular disk through a steel ball seated in an indented seat located so that the vertical load passed through the center of the bottom surface of the disk. With this arrangement little vertical rotation of the disk occurred during penetration.

Typical load-penetration curves of a 2-in. diameter disk for both level and sloping ground are shown in Figure 11. The results of a series of tests performed with 1-, $1\frac{1}{2}$-, and 2-in. disks on both level and 15-deg sloping beds of Jones Beach sand are given in Table 2. The ultimate loads (q_{ua}) were determined from the test results on the basis of tangency with $dq/dz = \gamma N_q$. The theoretical ultimate loads (q_{ut}) were determined using the stress gradient method described previously for the N_γ contribution and the actual depth of penetration at q_{ua} for the N_q fraction. The range of friction angle φ in Table 2 corresponds to those q_{ut} that bracket the experimentally obtained q_{ua}.

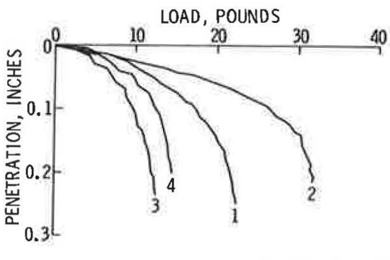

PLATE DIAMETER: 2 INCH

NO.	DENSITY (PCF)	SLOPE (DEGREES)
1	104.6	0
2	107.8	0
3	103.2	15
4	107.2	15

Figure 11. Results of small-scale tests.

TABLE 2

SUMMARY OF EXPERIMENTAL AND THEORETICAL RESULTS FOR ULTIMATE LOADS UNDER VARIOUS SIZED DISKS ON LEVEL AND SLOPING GROUND

Disk Diameter (in.)	ϵ = 0 deg				ϵ = 15 deg			
	γ (lb/cu ft)	q_{ua} (lb/sq in.)	q_{ut} (lb/sq in.)	φ (deg)	γ (lb/cu ft)	q_{ua} (lb/sq in.)	q_{ut} (lb/sq in.)	φ (deg)
1	104	3.38	3.08-3.71	42-43	103.6	1.43	1.27-1.52	42-43
	106.5	4.7	4.34-5.44	44-45	106.5	2.36	2.38	45
1½	102.5	4.7	4.33-5.22	42-43	102.5	3.32	3.31	45
	108.0	9.7	7.84-9.72	45-46	107.6	5.16	4.24-5.19	46-47
2	104.6	6.62	5.84-7.04	42-43	103.2	3.47	2.99-3.61	43-44
	107.8	10.0	8.92-10.96	44-45	107.2	4.14	3.66-4.47	44-45

A comparison of the back-computed friction angles φ for both the level (ϵ = 0) and sloped (ϵ = 15 deg) case indicates close correspondence. The fact that both computed values are slightly ($\approx$ 10 percent) larger than the value obtained from the triaxial data suggests a dependence of φ on strain conditions. The implications of using modified φ angles in bearing capacity formulas have been considered by others (5). The important point here is that the consistency in the back-computed friction angle φ between the level and sloped cases ensures the validity of the relative values of bearing strength between the two cases. As given in Table 2, with increase in slope there is in every case a substantial decrease in both the measured (q_{ua}) and predicted (q_{ut}) values for the ultimate bearing capacity.

CONCLUSIONS

In frictional soils where pore pressures are negligible, failure occurs in shear zones. For such soils the stability of slopes loaded over a finite area can be analyzed by bearing capacity methods. An approximate method has been developed assuming slip-line fields analogous to the Prandtl solution for horizontal ground. A formula for N_q for various slope angles and inclination of loads is given. In the case of slopes it is more convenient to express the effect of weight in terms of stress gradients, representing the rate of increase of bearing stresses from the edge of the loaded area, than by the N_q factor. Results of experiments performed on sand with small-diameter disks show that the bearing capacity on slopes can be reasonably well predicted by the approximate method.

REFERENCES

1. Meyerhof, G. G. The Ultimate Bearing Capacity of Foundations on Slopes. Proc. Fourth Internat. Conf. on Soil Mech. and Found. Engineering, Vol. 1, London, 1957.
2. Sokolovski, V. V. Statics of Soil Media. Butterworth and Co. Ltd., London, 1960.
3. Karafiath, L. L., and Nowatzki, E. A. A Study of the Effect of Sloping Ground on Bearing Strength and the Landing Performance of Space Vehicles. Grumman Aerospace Corp., Research Dept. Memo. RM-407, March 1968.
4. Harr, M. E. Foundations of Theoretical Soil Mechanics. McGraw-Hill, New York, 1966.
5. De Beer, E. E. Bearing Capacity and Settlement of Shallow Foundations on Sand. Proc. Symposium on Bearing Capacity and Settlement of Foundations, Duke Univ., Durham, N.C., 1967.

Appendix

NOTATION

The following symbols are used in this paper:

b = width of loading;
c = cohesion;
N_q, N_γ, N_c = bearing capacity factors;
p = surcharge;
q_u = ultimate unit load;
γ = unit weight;
σ = inclination of load measured from the vertical;
ϵ = slope angle;
θ = angle between x-axis and major principal stress;
λ = inclination of reduced surcharge measured from the vertical;
μ = $\pi/4 - \varphi/2$;
σ = $(\sigma_z + \sigma_x)/2 + \psi$
φ = friction angle; and
ψ = $c \cot \varphi$.